Uncovering log jamming in semi-dilute suspensions of quasi-ideal rods

Sergey Abakumov,[†] Olivier Deschaume,[‡] Carmen Bartic,[‡] Christian Lang,[¶] Olivera Korculanin,[§] Jan Karel George Dhont,[§] and Minne Paul Lettinga[*,§,‡]

[†]*Laboratory for Molecular Imaging and Photonics, KU Leuven, B-3001 Leuven, Belgium.*

[‡]*Laboratory for Soft Matter and Biophysics, KU Leuven, B-3001 Leuven, Belgium.*

[¶]*JCNS-4, Forschungzentrum Jülich, DE 85748 Jülich, Germany.*

[§]*IBI-4, Forschungzentrum Jülich, DE 52425 Jülich, Germany.*

E-mail: p.lettinga@fz-juelich.de

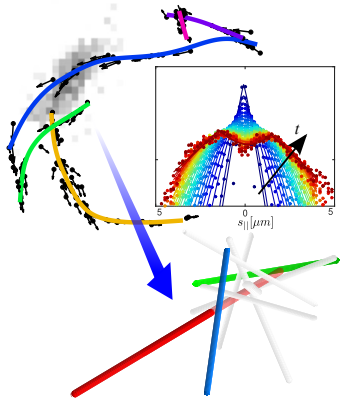

September 21, 2021

Abstract

Video microscopy on fluorescently labeled semi-flexible, slender, monodisperse colloidal rods in a host dispersion of unlabeled rods reveals a complex skating-type motion.

Trajectories of single rods consist of a zig-zag sequence of paths where rods move within a tube set up by the surrounding rods. We show that head-on collisions within the tube affect the dynamics in a fundamental way, leading to a unique anomalous splitting of the distribution of particle displacements. Based on this log jamming process and relatively weak tube confinement, we propose an improved coupling relation between the parallel and perpendicular motion of individual rods within a tube.

Introduction

The strongly hindered diffusion of entangled stiff polymers underlies their structural function in biological systems,[1–3] polymeric materials,[4] food products[5] and biomimetic hydrogels.[6,7] Thus, understanding the diffusive processes of rod-like macromolecules is a prerequisite for the design of material properties, and is fundamental to understand more complex systems, as stiff polymers have fewer degrees of freedom than regular polymers. In the late 1970s, Doi proposed a theory for rod diffusion based on geometrical arguments[8,9] and used it to determine the rheological response of rod dispersions.[10] Key to the Doi model is that rods are caged in a tube set by the surrounding rods, restricting the reorientational motion of the rod. In this model, rods can only rotate over a limited angle after translating half of their length out of the tube. An essential assumption in the theory is that this diffusion along the long axis of the rod is unhindered, as only very slender rods are considered. Though simulations tend to support the Doi model ,[11–14] the tube-concept has been debated ,[13,15–21] as well as the assumed free parallel diffusion.[13,22] Edwards and Evans (EE) added the possibility of head-on collisions between the rods and thereby derived a concentration dependent translational diffusion coefficient for motion along the long axis, which changes the dynamics in a qualitative way as compared to the original Doi theory. This log jamming model results in a glass transition at a location that depends on an unknown parameter .[22] In order to establish the origin of such a fundamentally different dynamics, it is necessary to be able to define tubes and to probe both the rotational and translational dynamics of

single rods within the tubes. We achieve this here by imaging the motion of monodisperse filamentous viruses, a model system for colloidal rods, by means of video microscopy. Such a single particle approach has been successfully exploited to characterize the anomalous motion in ordered phases.[23–25] We will show how sequencing of rod trajectories into tubes uncovers novel dynamics, confirming the concepts in the EE-theory and leading to a better understanding of averaged diffusion rates and the glass transition.

So far, experimental efforts supplied self or collective rotational and translational diffusion coefficients on a plethora of rod-like particles, using averaging techniques like dynamic light scattering, rheology, NMR, and fluorescence recovery after photobleaching.[26–33] Although these experiments confirmed the trend of the Doi model, deviations were found that could partly be attributed to flexibility of the systems. A more fundamental issue is that these ensemble averaging techniques do not allow to study the coupling between translation and rotation of the rods. For a full understanding it is a prerequisite to obtain the diffusion along and rotation of the long axis simultaneously, which requires imaging techniques. Imaging experiments on low aspect ratio ellipsoids confirmed the hydrodynamic relation between translation and rotation,[34] as well as a non-trivial coupling,[35] while high concentrations a sub-diffusive behavior was disclosed for low aspect ratio-rods,[36] similar to the caging dynamics of colloidal spheres.[37,38] Sub-diffusive behavior has also been found for high aspect ratio rod-shaped particles such as very slender filaments.[39–42] These studies focus, however, on the relaxation perpendicular to the imaginary tube. A study on rod-like grains in microgravity,[43] which approach the ideal system of slender rods, does discriminate in the direction of the motion, but with respect to mechanic excitation of the non- Brownian particles.

In this paper we first introduce the system of quasi-ideal rods, the imaging procedure of these rods and the analysis technique that we developed to identify the tubes and the motion within the tubes. We then discuss the dynamics within the tube and the new model that evolves from these results.

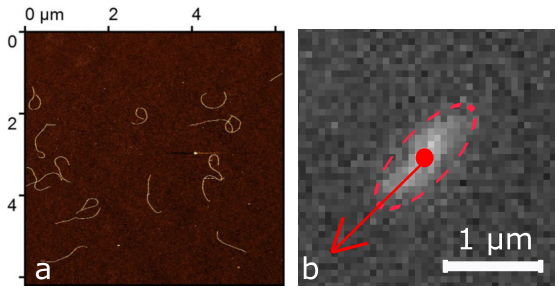

Figure 1: a) AFM images of M13k07. All rods were 1.2 μm in length. (b) Fluorescence image of M13k07. The arrow indicates the orientation obtained from the analysis.

Experimental

M13k07 has a contour length of $L = 1.2\ \mu m$, a persistence length of $l_p = 2.8\ \mu m$ and effective thickness of $d = 10\ nm$, when dispersed in a buffer of 100 mM NaCl and 20 mM Tris.[44] For our experiments we used the same batch of M13k07 as was used in Ref.[45] They were grown and purified using a standard protocol[46] and partly labeled (ratio 1:1000) with Alexa Fluor488 (ThermoFischer). The length was checked using atomic force microscopy (AFM, Agilent 5500 with MSNL-F cantilevers), see Fig. 1a, and confirmed to be 1.2 μm. We determined the concentration of the separated isotropic and nematic phases by UV-VIS. The isotropic-nematic binodal is located at 19.0 mg/ml, which is the predicted location for a rod with a contaour length of 1.2 μm and a persistence length of 2.8 μm.

We track the position and orientation of fluorescently labeled filamentous M13k07 viruses in dispersions of unlabeled viruses by means of fluorescence microscopy at concentrations up to the isotropic-nematic phase (I-N) transition at 19 mg/ml. For imaging, a Zeiss Axiovert microscope was equipped with a 100x NA 1.4 oil immersion objective, a Prizmatix LED lamp and an Andor sCMOS camera, running at frame rates between 10 and 100 fps, depending on the concentration. 10 μm latex beads were added to the suspension to fix the gap between the object glass and the cover slip and we focused the microscope in the middle of this gap.

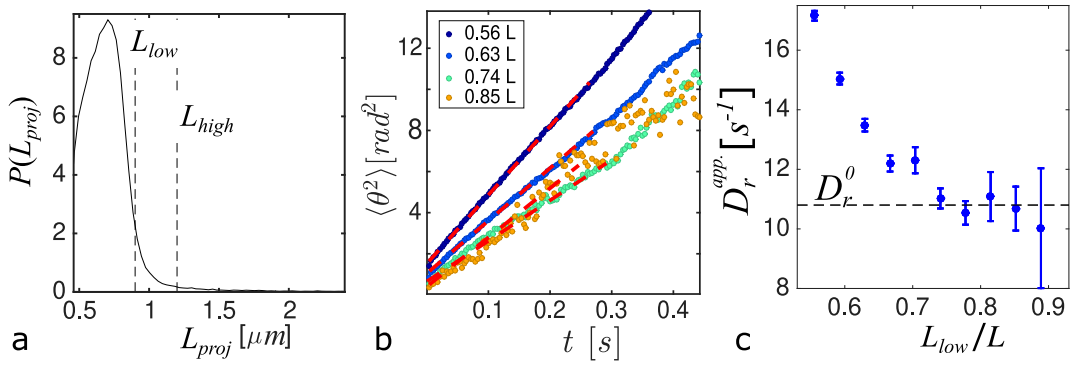

Figure 2: a) Distribution of projected lengths L_{proj} as detected by fluorescence microscopy. The vertical lines indicate the lower and upper boundaries of projected lengths selected for further analysis. (b) Mean square angular displacement for different projected lengths L_{low}. The dashed line is a linear fit. (c) Apparent rotational diffusion as function of L_{low}. The dashed line indicates the theoretical value.

Analysis

Particle orientation tracking

Due to the limited size of the rods, the particles appear as elongated blobs when imaged by florescent microscopy. The particles were first detected by thresholding the 2D image and detecting the blobs approximately. A square region of interest of the original image, see Fig. 1b, positioned around the blob, is fitted by a 2D Gaussian, defined as $A \exp -(x'-x_0)^2/2\sigma_x'^2 + (y-y_0)^2)/2\sigma_y'^2$, with (x_0, y_0) the coordinates defining the center-of-mass of the particle, $\sigma_{x',y'}$ the standard deviations respectively, and x', y' the coordinates of a frame rotated by angle θ, responsible for the orientation of the blob.

As the limited z-resolution precludes detection of their orientation in 3D, we refrained from full 3D analysis.[47] We access the dynamics by selecting the data of those trajectories where rods were oriented in the lateral plane, based on the imaged length of the rod. The imaged length was correlated to the largest blob width σ_{max} by simulating the optical diffracted image of an ideal M13k07. A full in-plane virus complies with $\sigma_{max} = 0.6\ L$. The isotropic distribution of rods results in a wide distribution of projected lengths L_{proj}, corresponding to the projections of the full length L in the plane of observation, see Fig. 2a.

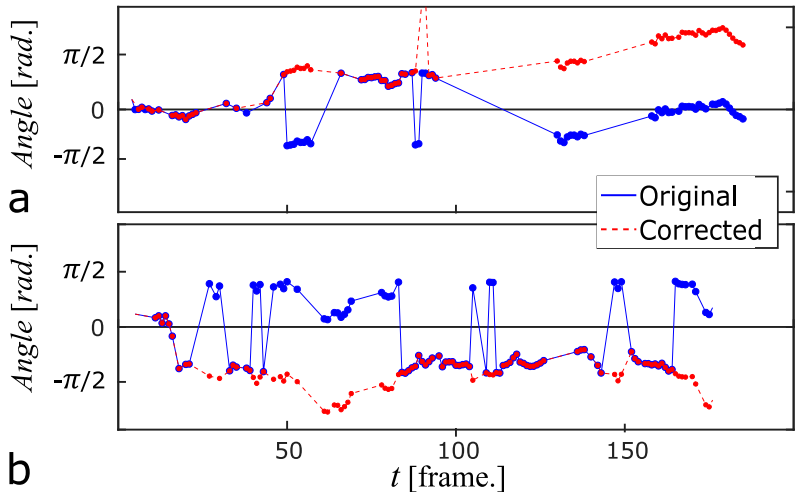

Figure 3: Results of angular trajectory reconstruction containing a jump (a), and a perfect trajectory reconstruction that passes the $\frac{\pi}{2}$ limit (b). The dots denote the datapoints used in the analysis, while the lines are a guide to the eye.

The trajectory is selected when $L_{low} < L_{proj} < L_{high}$, as indicated by the vertical lines in Fig. 2b, which depicts the size length distribution of L_{proj}. $L_{high} = L$ is chosen to remove the very sparse dimers from the analysis, although this analysis confirmed that the produced batch contained almost no dimers. The choice of L_{low} affects the determination of the rotational diffusion, as the accuracy of the detected in-plane angle depends on the aspect ratio of the blob. Indeed, the offset in the mean angular displacement at infinite dilution decreases with increasing L_{low}, see Fig. 2b. In addition, the apparent rotational diffusion constant, which is calculated from the slope, decreases with increasing L_{low}, see Fig. 2c. This is to be expected as the rotation of an out-of-plane rod by an angle θ of the long axis results in a bigger apparent projected angle $\theta_{obs} > \theta$ in the lateral observation plane. For $L_{low} > 0.75L$ a value of $D^0_{rot} = 11\ s^{-1}$, which is the same as the theoretical prediction for slender rods $D^0_{rot} = \frac{3k_BT}{\pi\eta_0 L^3} \ln \frac{L}{d}$, where d is the diameter of the rod, and η_0 the viscosity of the solvent.[48] This result confirms that with the restriction of selecting those rods that are oriented in the detection plane does not affect the final result. If too many rods are discarded, the statistics deteriorates. We therefore decided to use $L_{lower} = 0.75L_{high}$ as lower bound length. The number of tracked particles per concentration varied between 10^3 for low and

5×10^3 for high concentrations.

In determining the reorientational motion of the rods, we took the degeneracy in the detection of the angle into account. The orientation of a rod is determined in one quadrant, between $-\frac{\pi}{2}$ and $\frac{\pi}{2}$. A problem occurs when a rod rotates out of this quadrant into the neighbouring quadrant.

Although the actual rotation Δ might be very small, it will effectively undergo a jump of around $\pi - \Delta$. We resolved this issue by detecting the endpoints of the rod and tracking their movement. The endpoints were detected by skeletonizing the blob and determining the endpoints through an in-built Matlab routine. Depending on the displacement of these endpoints near the boundaries of the 1^{st} and the 2^{nd} quadrant, the transition between the quadrants can be identified and the full angular trajectory can be reconstructed. Despite the algorithm performing well on the majority of the trajectories ($> 95\%$), it was not error proof, as can be seen in Fig. 3a where a sudden jump occurs.

Tube extraction

At high concentrations, trajectories typically consist of a sequence of curved paths, which are connected at points where the trajectory becomes discontinuous as in a skating motion, see Fig. 4 and SI for movies. Analysis of the dynamics within the tubes in curvilinear coordinates is needed to understand the dynamics of the full trajectory, including jumps between tubes. We developed an algorithm to identify the sequence of tubes, allowing for such an analysis. Starting at time t_{start}, a cubic spline with a bending penalty, also known as a smoothing spline, $f(x)$ defined by the minimalization of the quantity $p \sum_i (y_i - f(x_i))^2 + \int f''(x)^2 dx$, where p is the smoothing factor, given as 10^{-3} in our analysis, was fitted through the trajectory up to time $t_{start+i}$ with the standard MATLAB procedure and the mean square error (MSE) was calculated. In order to obtain the best fit and to avoid multiple y-points for a single x point, the selected sequence was fitted for multiple rotations around its center of mass, and the orientation with the lowest MSE (measured in μm^2) was chosen. When

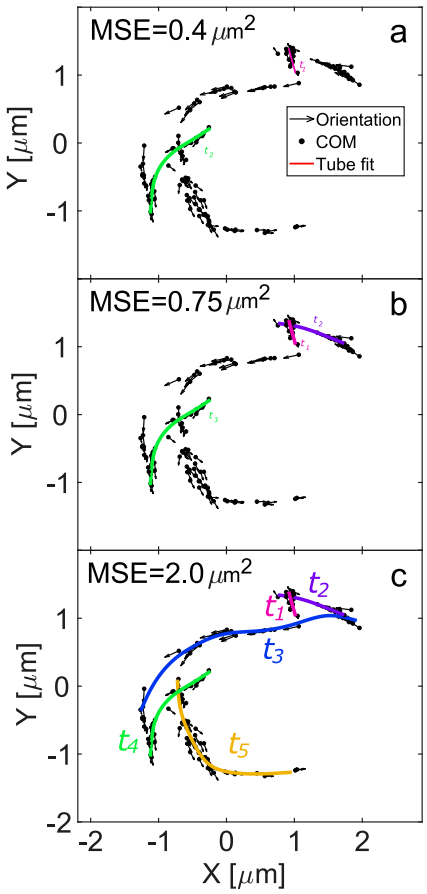

Figure 4: The efficiency of the tube detection in function of MSE filter (a to c). For the same trajectory, only stiffer tubes pass through the filter as the higher bound on the MSE becomes lower. The black arrows indicate the orientation of the rod at that point in time and the circles indicate the corresponding centre-of-mass (COM). The colored lines indicate the resolved tubes. In (c) we also indicate the order in time of the detected tubes, where $t_1 < t_2 < ...t_5$.

the resulting MSE was smaller than a preset threshold, then this point was identified as belonging to the same tube and the counter i was increased by 1. When MSE($t_{start+i}$) exceeded this value, then the trajectory between t_{start} and $t_{start+i-1}$ was stored as one tube and a new sequence was started at $t_{start+i}$. A next refining step was performed where a set of two sequential tubes were fitted again with a smoothing spline, recording MSE as a function of the split position n. The position n, where the sum of both errors was minimal, was set to be the branching point of the two tubes. By repeating the procedure on the full trajectory, we were able to separate the complex skating motion of a rod into a set of paths, where only

paths with a MSE smaller than the threshold value were assigned to a tube. The threshold value for MSE acts as a filter of the data, which influences the final results. The effect of the MSE filter on the tube selection is shown in Fig. 4, from which it follows that MSE=2.0 μm^2 is the best choice. In SI we show how the MSE threshold affects the results, giving a quantitative justification for our choice of MSE=2.0 μm^2 as threshold value.

This analysis yields the fraction of points within a trajectory that can be assigned to a tube, N_{tube}/N and the lifetime of the tube, τ_{tube}. Moreover, the motion of the rods can now be related to the dynamics within the the tube, as a set of curvilinear coordinates that define the motion parallel to the fitted spline $s_{||}$, so along the backbone of the tube, and the motion perpendicular to the fitted spline $s_{\perp}$, which probes the confinement of the tube. The definition of the coordinates are graphically depicted in Fig. 5.

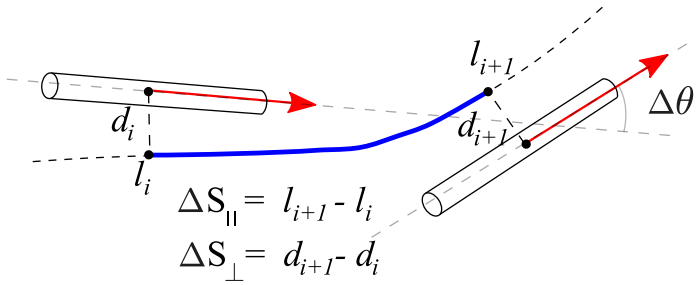

Figure 5: Definition of the curvilinear coordinates in a tube.

Results

Number of tubes and tube lifetime

The most prominent observation is the increasing persistence of the paths described by fluorescently labeled rod-like particles in a background of unlabeled particles with increasing concentration, see again SI for movies. These paths can be interpreted in terms of Doi's model, as the rotation is restricted by a confining tube set by the surrounding particles. The abrupt end of these tubes suggests that the rod in the tube undergoes a head-on collision with another rod and is reflected, as in the EE model. This kind of skating or zig-zag motion

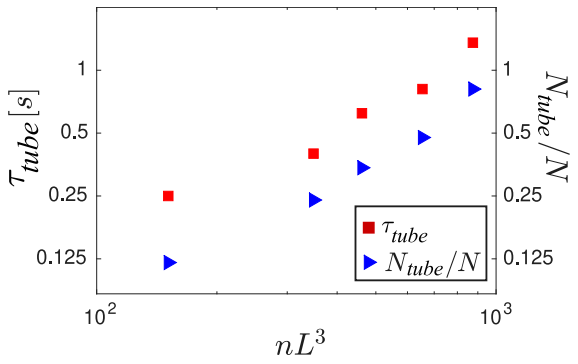

Figure 6: Ratio of points in a tubes over total number of points and average tube lifetime τ_{tube} vs. reduced concentration.

has been observed in simulations,[49,50] in experiments on needles through a network of 2D obstacles[51] and on carbon nano-tubes in a dense host system.[52] As indicated in the Analysis section, our analysis of these persistent paths in a trajectories results in the fraction of points within a trajectory that can be assigned to a tube, N_{tube}, over the total number of points in the trajectory N. In addition we obtain the lifetime of the tube, τ_{tube}. Both parameters are plotted as a function of concentration in Fig. 6. Clearly, more tubes can be identified and survive longer with increasing concentration. For $nL^3 < 100$ no tubes could be isolated, which means that there is a Limited range where tubes can be defined, which is a basic assumption in Doi theory.

Mean square displacement

The best way to compare the motion of the viral rods with other experimental work and simulations is by calculating the mean square displacements (MSD), $\langle r^2 \rangle$, and the mean square angular displacement (MSAD), $\langle \theta^2 \rangle_{full}$, of the full trajectory, as plotted in Fig. 7a and b, respectively. The motion of the rod-like viruses becomes increasingly restricted with increasing concentration. We quantify this slowing down by calculating the translational diffusion rate, D_t^{full}, and rotational diffusion rate, D_r^{full} from the initial slope of MSD and MSAD, respectively, where full refers to the calculation of diffusion rates by taking points from the entire trajectory of the particle, without explicit path determination and separation. D_r^{full} and

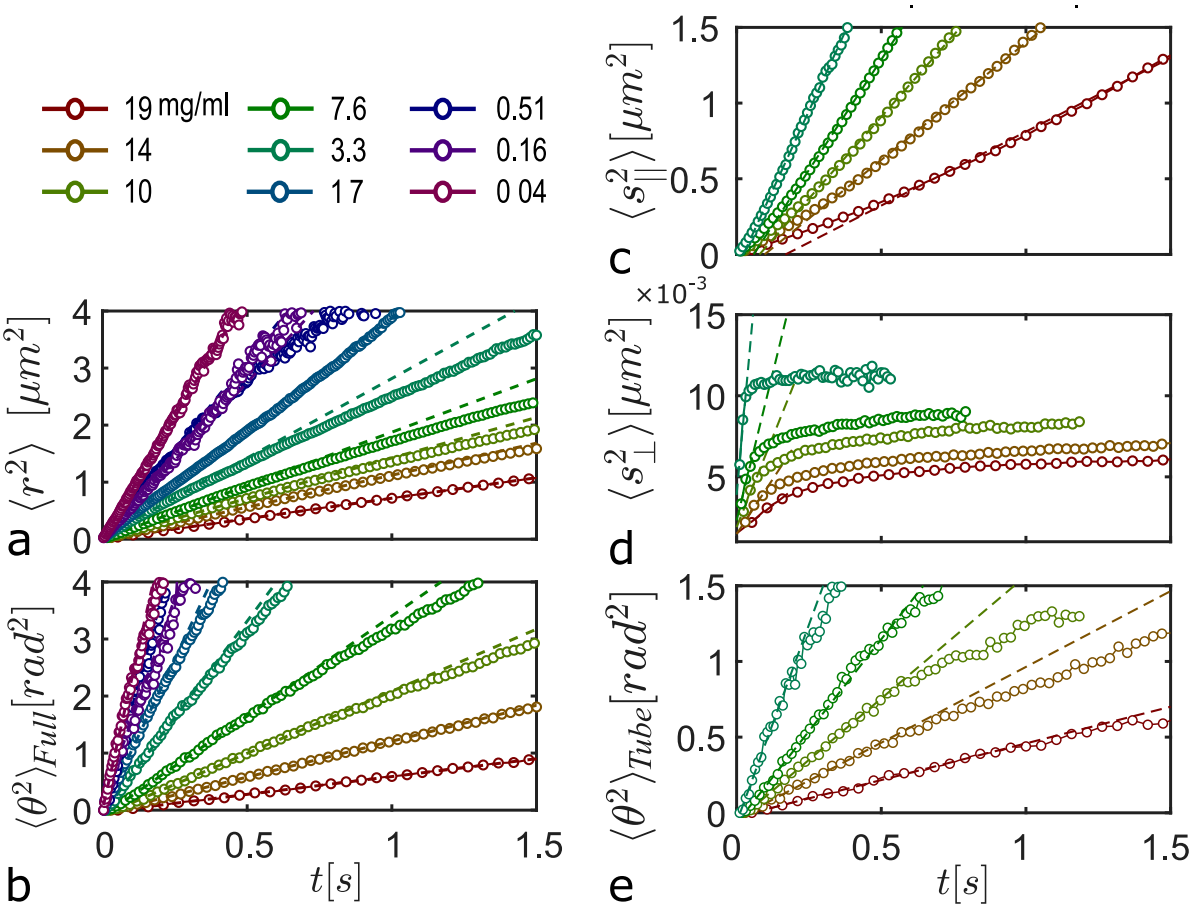

Figure 7: Translational (a) and angular (b) MSD from full trajectories. Parallel (c), perpendicular (d), and angular (e) MSD within the tube. Lines are fits to determine the diffusion coefficients. Note that in (b) and (e) we subtracted an offset of $\langle \theta^2 \rangle_{offset} \approx 0.3\ rad^2$, which is due to the error in the detection of the rod orientation.

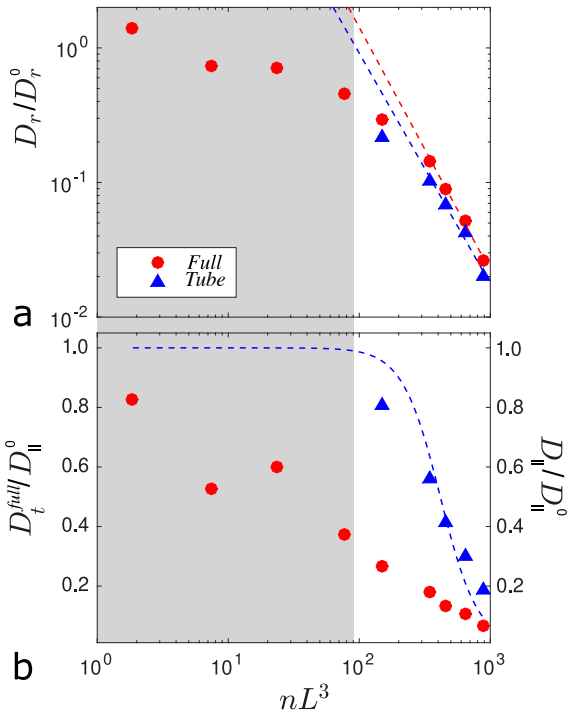

Figure 8: (a) D_r^{full} and D_r^{tube} vs. reduced concentration (lines are fits to Eq. 1); (b) D_t^{full} and $D_\parallel$ vs. reduced concentration (line is a fit to Eq. 7). The error bars are within the symbol size. The grey area indicates the concentration region where no tubes can be defined.

D_t^{full} gradually decreases with increasing concentration, see Fig. 8, similar to observations with averaging techniques for which MS(A)D is the only accessible parameter.[30–33]

In order to interpret the data we now know, however, that these parameters are averages over the rotation and translation due to the skating motion, and that the discrete jumps between the tubes affect the results. We therefore compare the results from the full trajectory with the results obtained within the tube, for which the MSD and MSAD are given in Fig. 7c-e. The rotational diffusion D_r we extract from the MSAD is plotted in Fig. 8a vs. nL^3, as Doi's model predicts the length L and number density n dependence of the rotational diffusion coefficient to be

$$D_r = CD_r^0(nL^3)^{-\gamma}. \tag{1}$$

Here D_r^0 is the rotational diffusion rate at infinite dilution and $\gamma \to 2$ in the limit of high concentrations where tubes can be defined. By fitting the data to Eq. 1, its validity is tested, yielding γ and the proportionality constant C . We find for the rotational diffusion within

the tube $\gamma = 1.7$ and $C = 2.8 \cdot 10^3$, and for the diffusion of the full trajectory we find $\gamma = 1.8$ and $C = 6.6 \cdot 10^3$. For the full trajectory, C is high because points are taken into account where no tube can be identified, see Fig. 6. In simulations $C \approx 1.3 \cdot 10^3$ was found,[12,53] as well as by rheological experiments on a library of rod-like viruses.[45] The somewhat lower value for γ than the Doi prediction is mainly due to the limited linear regime. This also seems to hold for the simulations,[12–14,18] though much higher values for nL^3 can be reached for infinitely thin rods as these do not display a I-N phase transition. More importantly, the rigid tube diameter in Doi's model[15,20,21,54] and the effect of the finite thickness of the rods[13,22] have been debated. As we can identify dynamics within a tube, we are able to elucidate this discussion.

The observation of a skating motion suggests that Doi's assumption of unhindered parallel diffusion is not valid. This assumption can be directly tested as we isolated the diffusion along the contour of a tube, given by $s_\parallel$. $\langle s_\parallel^2 \rangle$ is initially sub-diffusive, and becomes diffusive after some time τ_{lin}, see Fig. 7c. This behavior is typical for glassy systems and is associated with the relaxation into the long-time diffusion regime after particles have escaped the cage of surrounding particles.[38] We extract the parallel diffusion rate $D_\parallel$ within the tube from the final slope in $\langle s_\parallel^2 \rangle$, see Fig. 7c, and find that $D_\parallel$ is indeed smaller than the infinite dilute parallel diffusion rate $D_\parallel^0$ and decreases with increasing concentration, see Fig. 8b.

Self-van Hove functions

MSDs are the average $\langle q^2(t) \rangle = \int dq\, q^2 G(q,t)$ over the time-dependent conditional probability $G(q,t)$ to find a particle at time t at a position/angle q, given that at $t = 0$, $q = 0$. This is the so-called Self-van Hove function (SvH). $G(q,t)$ can be directly extracted from particle positions or angles and contains more information than the averaged $\langle q^2(t) \rangle$, as we will now discuss. The $G(s_\parallel, t)$ for the parallel displacement within a tube shows a very interesting effect, namely the development of a minimum at the origin ($s_\parallel = 0$), see Fig. 9a. This means that there is directionality in the movement. If one considers a rod that is restricted in its

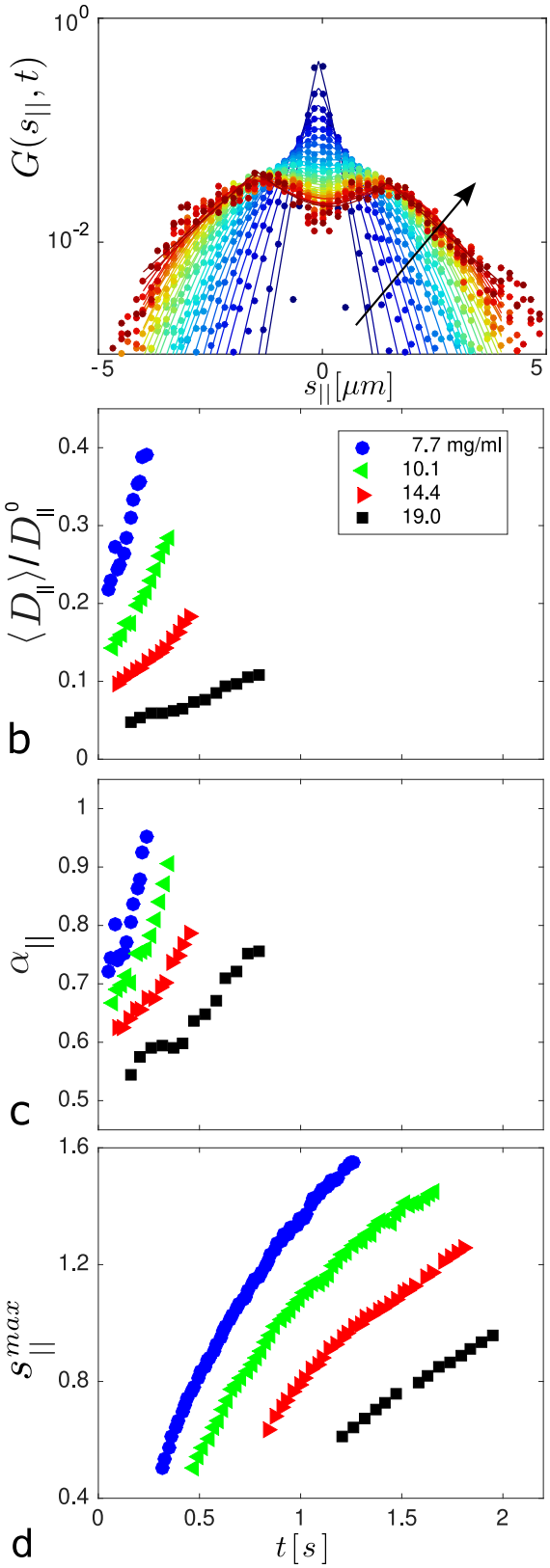

Figure 9: (a) Evolution of the $G(s_{\|}, t)$ for 14 mg/ml, fitted with Eq. 2. The arrow indicates the order in time, while curves were calculated with a time spacing of $\Delta t = 70$ ms. (b-d) Fit results vs time: the scaled averaged diffusion rate $\langle D_{\|} \rangle / D_{\|}^0$ (b); the exponent $\alpha_{\|}$ (c); the position of the maximum $s_{\|}^{max}$ (d).

motion only at one end of a tube by a blocking rod, than the probability of finding a particle in this direction of the original position is less then to the other, free direction. This will result in a skewed, off-centered distribution. As the problem is symmetric, a minimum will evolve in the center.

Whilst the splitting is certainly a result of the identification of the tubes, see Fig. 4, jamming events can also take place within the tube, contributing to the skewed distributions. This is the case when the relaxation time of the jamming, τ_{relax}, is shorter than the time to find another tube. Jamming events result in a distribution of diffusion rates, leading to Laplacian dynamics when probing $G(s_\parallel, t)$ on the timescale of the relaxation time τ_{relax}, while for much longer times $G(s_\parallel, t)$ should evolve to a Gaussian.[55,56] From the above it follows that jamming will contribute both to the splitting as well as non-Gaussian behavior of the $G(s_\parallel, t)$. Therefore we fit the data with a function

$$G(s_\parallel, t) = C\Big(\exp -(\frac{(s_\parallel - s_\parallel^{max})^2}{4\langle D_\parallel \rangle t})^{\alpha_\parallel} + \exp -(\frac{(s_\parallel + s_\parallel^{max})^2}{4\langle D_\parallel \rangle t})^{\alpha_\parallel} \Big) \tag{2}$$

that smoothly connects purely Gaussian dynamics, $\alpha_\parallel \to 1$, with Laplacian dynamics, $\alpha_\parallel \to 0.5$, but that also describes the splitting, introducing $s_\parallel^{max}$ as the position of the maximum. The brackets $\langle ... \rangle$ indicated an averaging over the instantaneous distribution of diffusion rates at time t. C is a normalization constant. As can be seen in Fig. 9a, the date is well described by the function. Note also that the shape of Eq. 2 resembles the starting equation in the EE-theory.

As expected, we observe that both $\langle D_\parallel \rangle / D_\parallel^0$, Fig. 9b, and the exponent $\alpha_\parallel$, Fig. 9c, are initially very low and more so with increasing concentration. For the lowest concentration where we could identify tubes, the dynamics almost relaxes to Gaussian. $\langle D_\parallel \rangle / D_\parallel^0$ almost relaxes to the value obtained from $\langle s_\parallel^2 \rangle$, see Fig. 8b, which is still not completely free. $\langle D_\parallel \rangle / D_\parallel^0$ and $\alpha_\parallel$ are not accessible for longer times as splitting becomes too pronounced. At the highest concentration we find initially $\alpha_\parallel \approx 0.5$ and slow relaxation. The relaxation of these parameters indeed seems to be correlated with the tube lifetime displayed in Fig. 6

and gives a more detailed view on the initial sub-diffusive behavior of $\langle s_{\parallel}^2 \rangle$, see Fig.7c. Note however, that a linear time-dependence of $\langle s_{\parallel}^2 \rangle$ is reached even though the dynamics is still non-Gaussian with $\alpha_{\parallel} < 1$, as has also been observed for many other complex fluids.[42] The peak separation s_{max} increases with time, see Figs. 9d and S2. It cannot be determined at short times though it sets in immediately, as we learn from extrapolating $s_{\parallel}^{max}(t \to 0)$. s_{max}

.

$G(r,t)$ of the full trajectory, plotted in Fig. 10a, does not show the anomalous splitting, so $r_{max} = 0$. It does show more strongly non-Gaussian dynamics, Fig. 10c, as compared to the dynamics within the tube, Fig. 9c, so $\alpha_t < \alpha_{\parallel}$. The reason is that the dynamics does now not depend only on blocking and relaxation events within the tube, but also on the rotation that a rod undergoes when it jumps from one tubes into another, which randomizes the direction of translation. Again, though $\langle r^2(t) \rangle$ is linear, $\alpha_t < 1$ so the dynamics is non-Gaussian. This is similar to observations in simulations[14] and experiments like mechanically excited granular rods[43] and very similar to rod-like viruses in polymer solutions.[57] Values of $\alpha_t < 1$ can be attributed to a distribution in diffusion rates,[56] which is clearly the case when analysing full trajectories as in these references.

With our analysis, where we split up the full trajectory in tube-segments, we indeed identify the different contributions as we disentangled the diffusion along the long axis of the rod from the jump between tubes. The distributions do relax towards Gaussian dynamics where $\alpha_t \to 1$, Fig. 10c, along with the averaged diffusion rate $\langle D_t^{full} \rangle$, Fig. 10b, which approaches the value obtained from $\langle r^2 \rangle$. This relaxation is related with the number of re-orientations of the rod. However, $\alpha_t = 1$ is never reached even for low concentrations, due to the limited statistics at the long times needed for complete randomization.

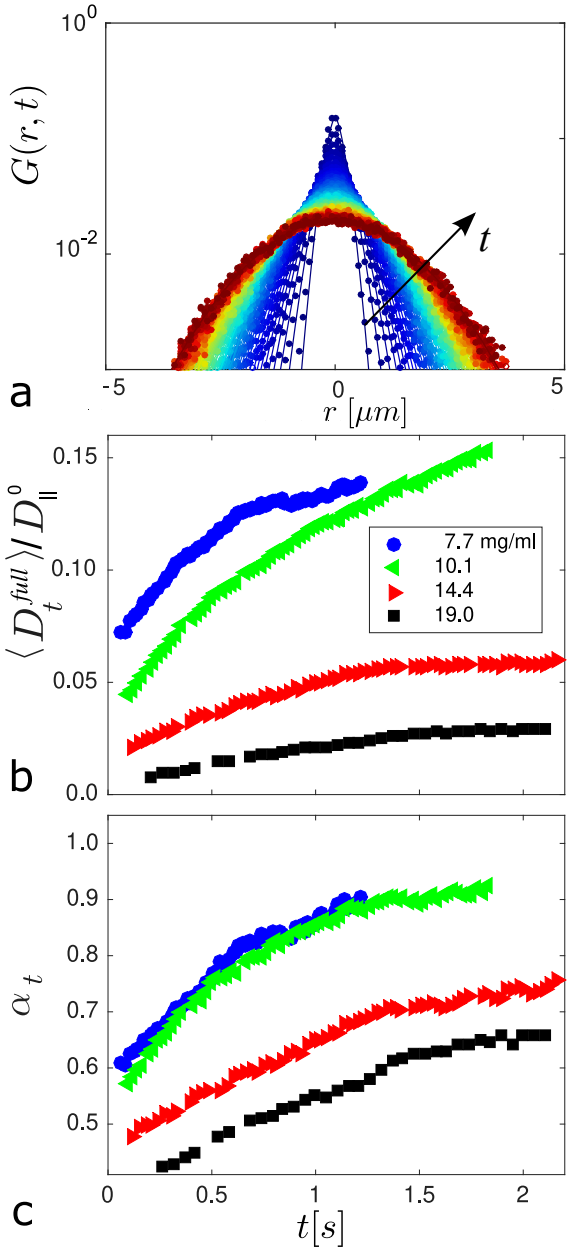

Figure 10: (a) Evolution of the $G(r,t)$ for 14 mg/ml, fitted with Eq. 2. The arrow indicates the order in time, while curves were calculated with a time spacing of $\Delta t = 70$ ms. (b,c) Fit results vs time: diffusivity parameter $\langle D_t^{full} \rangle$ (b) and exponent of the translational motion α_t (c).

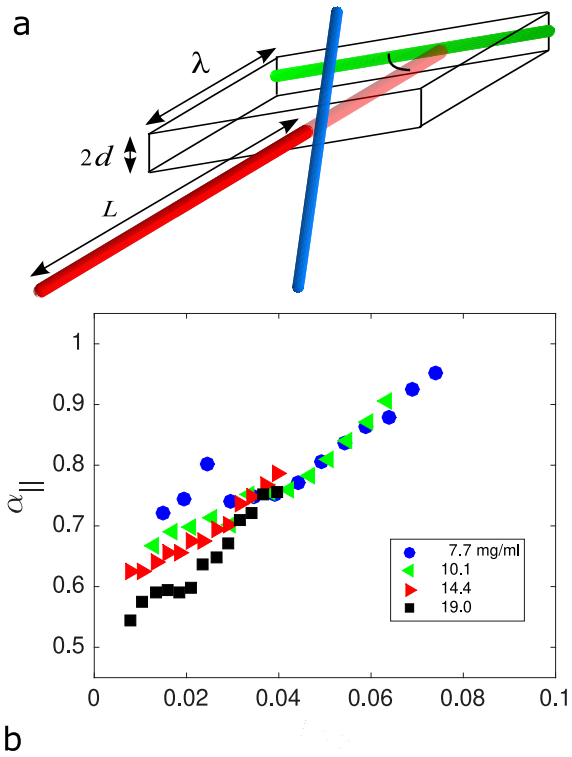

Figure 11: (a) Cartoon of a head-on collision and the connected geometry. (b) Scaling the relaxation in exponent $\alpha_{\|}$, see Fig. 9c, with the calculated τ_b, Eq. 5.

Discussion: adjusted Edwards-Evans model

The heterogeneity in the dynamics as identified by the self-van Hove function for the isolated tubes, combined with the abrupt ends of the tubes, suggest that the rods are confined by Doi tubes and undergo log jamming, where the head of the rods hits the side of another rod that crosses the tube. Slowing down of the dynamics could in principle also be caused purely by an increase in the hydrodynamic interactions. This would not lead, however, to a more pronounced heterogeneity. Moreover, it has been shown that hydrodynamic interactions for such slender rods in the isotropic phase hardly affect the diffusion.[24] The notion of log jamming for high aspect ratio rods might seem counter intuitive and therefore we investigate if the slowing down of the parallel diffusion $D_{\|}$, predicted by the EE model, is realistic. In this model, the concentration dependence of $D_{\|}$ is given by

$$D_{\parallel} = D_{\parallel}^{0}(1 + g\rho_b L\tau_{relax})^{-1}, \tag{3}$$

where g is a constant, ρ_b is the number of barriers per unit length per time, and τ_{relax} is the time it takes for the barrier to relax. We derive ρ_b by calculating the mean free pathway λ between two blocking rods, as illustrated by the blue en green rod in Fig. 11a, assuming that very slender particles can only be blocked by a side collision with another particle. If we consider that any direct interaction with the particle surface results in an effective jamming, then the total interaction area of two rods is given by $S_{int} = 2Ld\cos(\theta)$, where θ is the angle between the long-axis of the particles and d the particle thickness, see Fig. 11a. The definition of the mean free pathway λ implies that the volume $V = S_{int}\lambda$ contains on average 1 particle, so that $nV = 1$. Averaging the interaction surface over the angle, we obtain $\langle S_{int}\rangle = \frac{4Ld}{\pi}$, so that

$$\lambda = \frac{\pi}{4nLd}. \tag{4}$$

The average time between two head-on collisions is then given by

$$\tau_b = \frac{\lambda^2}{2D_{\parallel}^{0}}. \tag{5}$$

We test the viability of this approach, assuming that the relaxation in $\alpha_{\parallel}$, see Fig. 9c, is due to the rate at which the distribution of diffusion rates relaxes, as described in Ref.[56] This rate is low when the frequency of blocking events, causing also the distribution in diffusion rates, is high. As this frequency increases with increasing concentration, we scale time by $1/\tau_b$, which is purely based on the geometry and concentration of the rods. Indeed, we see now in Fig. 11b that all curves of $\alpha_{\parallel}$ vs $t\ \tau_b$ overlay. This confirms that head-on collisions

slow down dynamics so that we can write for ρ_b

$$\rho_b = \frac{2D_{\parallel}^0}{\lambda^3}. \tag{6}$$

Next, we need to identify the relaxation time of the tube, τ_{relax}. In the EE model, the relaxation mechanism is due to parallel diffusion of the blocking rod over its full length, which suggests that there is no significant perpendicular diffusion. We indeed observe that the perpendicular diffusion levels off, confirming the presence of an effective tube. However, the plateau that is reached exceeds the rod diameter by at least one order of magnitude, see Fig. 7b, and is thus much bigger than the $1/nL^2$ suggested by Doi. Although the increased effective tube diameter could be due to flexibility,[19,20,40,58] there are many arguments in favor of a less constraining tube.[14,16,20,21,54] Hence, we propose a perpendicular diffusive relaxation mechanism needed to overcome the barrier. This relaxation mechanism can be described by the relaxation time $\tau_{relax} = \frac{d^2}{2D_{\perp}^{seg}}$, where $D_{\perp}^{seg}$ is the perpendicular diffusion rate of the segment at the tip of the virus, which can either be due to flexibility or perpendicular diffusion.[20,52] This relaxation is much faster than suggested by the EE model. We now find

$$D_{\parallel} = D_{\parallel}^0 \left(1 + \ (\frac{4}{\pi})^3 g \ n^{*3} p^{-5} \frac{D_{\parallel}^0}{D_{\perp}^{seg}}\right)^{-1}, \tag{7}$$

where we introduced the overlap concentration $n^* = L^3 n$ and the aspect ratio $p = L/d$.

Eq. 7 is an insightful relation as it shows an extreme dependence on the aspect ratio, which competes with an inverted dependence on the overlap concentration. In the limit of infinitely thin rods, the equation reduces to $D_{\parallel} = D_{\parallel}^0$, so the Doi limit is recovered. The dynamics freezes when the tube diameter approaches the rod diameter, so $D_{\parallel} \to 0$. Thus, Eq. 7 also gives a dynamic criterion for a glass transition of rods, complementing earlier static definitions .[59,60] A fit of $D_{\parallel}$ vs nL^3 with Eq. 7, see Fig. 8b, yields $g\frac{D_{\parallel}^0}{D_{\perp}^{seg}} \approx 170$. Given the assumptions made in the theory, we consider this result to be a direct indication of the diffusion mechanism within the tube. With $g = \mathcal{O}(1)$ from the EE model, we find

$D_{\perp}^{seg} = \mathcal{O}(10^{-2}\ D_{\perp}^{0})$. This shows a significant slowing down even though the tube diameter, which we obtain from the plateau values in Fig. 7d, only decreases down to $\approx$ 70 nm, which is still much larger than the rod diameter. To complete the picture, it would be helpful to conduct simulations on slender rods in order to identify log jamming events and to revisit theories on the tube diameter.

Conclusion

In conclusion, disentangling trajectories of fluorescent semi-flexible monodisperse colloidal rods in semi-dilute dispersion elucidates an anomalous splitting in the distribution of the particle displacement along the isolated tubes. The slowing down of the parallel diffusion within a confining tube due to the underlying log jamming motivated the formulation of a non-trivial coupling relation between the parallel and perpendicular motion. This relation can be used to predict a dynamic glass transition for many emerging macromolecular systems.

Associated content

Supporting Information Available: The following files are available free of charge. File name. It contains 1) additional information concerning the effect of the MSE threshold on the resulting extracted diffusion parameters. Movies M13-conc0.04.avi, Movie M13-conc7.7.avi and M13-conc19.avi are real time video microscopy movies of fluorescently labeled viruses moving in a dispersions of 0.04, 7.7 and 19 mg/ml of unlabeled viruses, respectively.

Acknowledgement

O.K. acknowledges the International Helmholtz Research School of Biophysics and Soft Matter for financial support. C. L. acknowledges the European Union within the Horizon 2020

project under the DiStruc Marie Skłodowska Curie innovative training network; grant agreement no. 641839.

References

(1) Olson, M. F.; Sahai, E. The actin cytoskeleton in cancer cell motility. Clinical & Experimental Metastasis **2009**, 26, 273–287.

(2) Maji, S. K.; Perrin, M. H.; Sawaya, M. R.; Jessberger, S.; Vadodaria, K.; Rissman, R. A.; Singru, P. S.; Nilsson, K. P. R.; Simon, R.; Schubert, D.; Eisenberg, D.; Rivier, J.; Sawchenko, P.; Vale, W.; Riek, R. Functional Amyloids As Natural Storage of Peptide Hormones in Pituitary Secretory Granules. Science **2009**, 325, 328–332.

(3) Stricker, J.; Falzone, T.; Gardel, M. L. Mechanics of the F-actin cytoskeleton. Journal of Biomechanics **2010**, 43, 9–14.

(4) Picken, S. J.; Aerts, J.; Visser, R.; Northolt, M. G. Structure and Rheology of Aramid Solutions - X-Ray-Scattering Measurements. Macromolecules **1990**, 23, 3849–3854.

(5) van der Linden, E.; Venema, P. Self-assembly and aggregation of proteins. Current Opinion in Colloid & Interface Science **2007**, 12, 158–165.

(6) Kouwer, P. H. J.; Koepf, M.; Le Sage, V. A. A.; Jaspers, M.; van Buul, A. M.; Eksteen-Akeroyd, Z. H.; Woltinge, T.; Schwartz, E.; Kitto, H. J.; Hoogenboom, R.; Picken, S. J.; Nolte, R. J. M.; Mendes, E.; Rowan, A. E. Responsive biomimetic networks from polyisocyanopeptide hydrogels. Nature **2013**, 493, 651–655.

(7) Ruter, A.; Kuczera, S.; Gentile, L.; Olsson, U. Arrested dynamics in a model peptide hydrogel system. Soft Matter **2020**, 16, 2642–2651.

(8) Doi, M. ROTATIONAL RELAXATION-TIME OF RIGID ROD-LIKE MACROMOLECULE IN CONCENTRATED SOLUTION. J. de Physique **1975**, 36, 607–611.

(9) Doi, M.; Edwards, S. F. Dynamics of Rod-like Macromolecules in Concentrated Solution Part 2. J. Chem. Soc., Faraday Trans. II **1978**, 74, 918–932.

(10) Doi, M. Molecular-Dynamics and Rheological Properties of Concentrated-Solutions of Rodlike Polymers in Isotropic and Liquid-Crystalline Phases. Journal of Polymer Science Part B-Polymer Physics **1981**, 19, 229–243.

(11) Doi, M.; Yamamoto, I.; Kano, F. Monte Carlo Simulation of the Dynamics of Thin Rodlike Polymers in Concentrated Solution. J. Phys. Soc. Jpn. **1984**, 53, 3000–3003.

(12) Tao, Y. G.; Dhont, J. K. G.; Briels, W. J. Isotropic-nematic spinodals of rigid long thin rodlike colloids by event-driven Brownian dynamics simulations. J. Chem. Phys. **2006**, 124.

(13) Cobb, P. D.; Butler, J. E. Simulations of concentrated suspensions of rigid fibers: Relationship between short-time diffusivities and the long-time rotational diffusion. J. Chem. Phys. **2005**, 123, 054908.

(14) Leitmann, S.; Hofling, F.; Franosch, T. Dynamically crowded solutions of infinitely thin Brownian needles. Physical Review E **2017**, 96.

(15) Fixman, M. Entanglements of Semidilute Polymer Rods. Physical Review Letters **1985**, 54, 337–339.

(16) Fixman, M. Dynamics of Semidilute Polymer Rods: An Alternative to Cages. Phys. Rev. Lett. **1985**, 55, 2429–2432.

(17) Bitsanis, I.; Davis, H. T.; Tirrell, M. Brownian Dynamics of Nondilute Solutions of Rodlike Polymers .1. Low Concentrations. Macromolecules **1988**, 21, 2824–2835.

(18) Bitsanis, I.; Davis, H. T.; Tirrell, M. Brownian Dynamics of Nondilute Solutions of Rodlike Polymers. 2. High Concentrations. Macromolecules **1990**, 23, 1157–1165.

(19) Sato, T.; Takada, Y.; Teramoto, A. Dynamics of Stiff-Chain Polymers in Isotropic Solution .3. Flexibility Effect. Macromolecules **1991**, 24, 6220–6226.

(20) Odijk, T. On the Statistics and Dynamics of Confined or Entangled Stiff Polymers. Macromolecules **1983**, 16, 1340–1344.

(21) Teraoka, I.; Hayakawa, R. Theory of dynamics of entangled rod-like polymers by use of a mean-field Green function formulation. I. Transverse diffusion. J. Chem. Phys. **1988**, 89, 6989–6995.

(22) Edwards, S. F.; Evans, K. E. Dynamics of Highly Entangled Rod-like Molecules. J. Chem. SOC., Faraday Trans. 2 **1982**, 78, 113–121.

(23) Lettinga, M. P.; Barry, E.; Dogic, Z. Self-diffusion of rod-like viruses in the nematic phase. Europhys. Lett. **2005**, 71, 692–698.

(24) Lettinga, M. P.; Dhont, J. K. G.; Zhang, Z.; Messlinger, S.; Gompper, G. Hydrodynamic interactions in rod suspensions with orientational ordering. Soft Matter **2010**, 6, 4556–4562.

(25) Pouget, E.; Grelet, E.; Lettinga, M. P. Dynamics in the smectic phase of stiff viral rods. Phys Rev E Stat Nonlin Soft Matter Phys **2011**, 84, 041704.

(26) King, T. A.; Knox, A.; Mcadam, J. D. G. Translational and Rotational Diffusion of Tobacco Mosaic-Virus from Polarized and Depolarized Light-Scattering. Biopolymers **1973**, 12, 1917–1926.

(27) Phalakornkul, J. K.; Gast, A. P.; Pecora, R. Rotational and Translational Dynamics of Rodlike Polymers: A Combined Transient Electric Birefringence and Dynamic Light Scattering Study. Macromolecules **1999**, 32, 3122–3135.

(28) Lehner, D.; Lindner, H.; Glatter, O. Determination of the translational and rotational

diffusion coefficients of rodlike particles using depolarized dynamic light scattering. Langmuir **2000**, 16, 1689–1695.

(29) Brouzet, C.; Mittal, N.; Soderberg, L. D.; Lundell, F. Size-Dependent Orientational Dynamics of Brownian Nanorods. Acs Macro Letters **2018**, 7, 1022–1027.

(30) Cush, R. C.; Russo, P. S. Self-diffusion of a rodlike virus in the isotropic phase. Macromolecules **2002**, 35, 8659–8662.

(31) Petekidis, G.; Vlassopoulos, D.; Fytas, G.; Fleischer, G.; Wegner, G. Dynamics of wormlike polymers in solution: Self-diffusion and zero-shear viscosity. Macromolecules **2000**, 33, 9630–9640.

(32) Cassagnau, P.; Zhang, W. J.; Charleux, B. Viscosity and dynamics of nanorod (carbon nanotubes, cellulose whiskers, stiff polymers and polymer fibers) suspensions. Rheologica Acta **2013**, 52, 815–822.

(33) Rosu, C.; von Meerwall, E.; Russo, P. S. Diffusion of Rodlike Polymers: Pulsed Gradient Spin Echo NMR of Poly(gamma-stearyl-alpha,L-glutamate) Solutions and the Importance of Helix Stability. Journal of Physical Chemistry B **2018**, 122, 12194–12200.

(34) Mukhija, D.; Solomon, M. J. Translational and rotational dynamics of colloidal rods by direct visualization with confocal microscopy. Journal of Colloid and Interface Science **2007**, 314, 98–106.

(35) Han, Y.; Alsayed, A. M.; Nobili, M.; Zhang, J.; Lubensky, T. C.; Yodh, A. G. Brownian motion of an ellipsoid. Science **2006**, 314, 626–630.

(36) Maeda, A.; Maeda, Y. Direct Observation of Brownian Dynamics of Hard Colloidal Nanorods. Nano Letters **2007**, 7, 3329–3335.

(37) Cipelletti, L.; Ramos, L. Slow dynamics in glassy soft matter. Journal of Physics-Condensed Matter **2005**, 17, R253–R285.

(38) Weeks, E. R.; Crocker, J. C.; Levitt, A. C.; Schofield, A.; Weitz, D. A. Three-dimensional direct imaging of structural relaxation near the colloidal glass transition. Science **2000**, 287, 627–631.

(39) Kas, J.; Strey, H.; Sackmann, E. Direct Imaging of Reptation for Semiflexible Actin-Filaments. Nature **1994**, 368, 226–229.

(40) Keshavarz, M.;Engelkamp, H.; Xu, J.; Braeken, E.; Otten, M.B.J.; Uji-i„ H.; Schwartz, E.; Koepf, M.; Vananroye, A.; Vermant, J.; Nolte, R.J.M.; De Schryver, F.; Maan, J.C.; Hofkens, J.; Christianen, P.C.M.; Rowan, A.E. Nanoscale Study of Polymer Dynamics. Nanoscale Study of Polymer Dynamics. Acs Nano **2016**, 10, 1434–1441.

(41) Wang, B.; Guan, J.; Anthony, S. M.; Bae, S. C.; Schweizer, K. S.; Granick, S. Confining Potential when a Biopolymer Filament Reptates. Physical Review Letters **2010**, 104.

(42) Wang, B.; Kuo, J.; Bae, S. C.; Granick, S. When Brownian diffusion is not Gaussian. Nature Materials **2012**, 11, 481–485.

(43) Harth, K.; Kornek, U.; Trittel, T.; Strachauer, U.; Home, S.; Will, K.; Stannarius, R. Granular Gases of Rod-Shaped Grains in Microgravity. Physical Review Letters **2013**, 110.

(44) Alvarez, L.; Lettinga, M. P.; Grelet, E. Fast Diffusion of Long Guest Rods in a Lamellar Phase of Short Host Particles. Phys Rev Lett **2017**, 118, 178002.

(45) Lang, C.; Kohlbrecher, J.; Porcar, L.; Raclulescu, A.; Sellinghoff, K.; Dhont, J. K. G.; Lettinga, M. P. Microstructural Understanding of the Length- and Stiffness-Dependent Shear Thinning in Semidilute Colloidal Rods. Macromolecules **2019**, 52, 9604–9612.

(46) Sambrook, J.; Fritsch, E. F.; Maniatis, T. Molecular Cloning: A Laboratory Manual; Cold Spring Harbor Laboratory Press, 1989.

(47) Besseling, T. H.; Hermes, M.; Kuijk, A.; de Nijs, B.; Deng, T. S.; Dijkstra, M.; Imhof, A.; van Blaaderen, A. Determination of the positions and orientations of concentrated rod-like colloids from 3D microscopy data. Journal of Physics-Condensed Matter **2015**, 27.

(48) Burgers, J. M. Second report on viscosity and plasticity, Amsterdam Academy of Science; Nordeman, Amsterdam, 1938; p 3.

(49) Hofling, F.; Frey, E.; Franosch, T. Enhanced diffusion of a needle in a planar array of point obstacles. Physical Review Letters **2008**, 101.

(50) Hofling, F.; Munk, T.; Frey, E.; Franosch, T. Entangled dynamics of a stiff polymer. Physical Review E **2008**, 77.

(51) Kasimov, D.; Admon, T.; Roichman, Y. Diffusion of a nanowire rod through an obstacle field. Physical Review E **2016**, 93.

(52) Fakhri, N.; Wessel, A. D.; Willms, C.; Pasquali, M.; Klopfenstein, D. R.; MacKintosh, F. C.; Schmidt, C. F. High-resolution mapping of intracellular fluctuations using carbon nanotubes. Science **2014**, 344, 1031–1035.

(53) Teraoka, I.; Ookubo, N.; Hayakawa, R. Molecular Theory on the Entanglement Effect of Rodlike Polymers. Physical Review Letters **1985**, 55, 2712–2715.

(54) Sussman, D. M.; Schweizer, K. S. Microscopic Theory of the Tube Confinement Potential for Liquids of Topologically Entangled Rigid Macromolecules. Physical Review Letters **2011**, 107.

(55) Chechkin, A. V.; Seno, F.; Metzler, R.; Sokolov, I. M. Brownian yet Non-Gaussian Diffusion: From Superstatistics to Subordination of Diffusing Diffusivities. Physical Review X **2017**, 7, 021002.

(56) Chubynsky, M. V.; Slater, G. W. Diffusing Diffusivity: A Model for Anomalous, yet Brownian, Diffusion. Physical Review Letters **2014**, 113, 098302.

(57) Smith, M.; Poling-Skutvik, R.; Slim, A. H.; Willson, R. C.; Conrad, J. C. Dynamics of Flexible Viruses in Polymer Solutions. Macromolecules **2021**, 54, 4557–4563.

(58) Wang, B.; Anthony, S. M.; Bae, S. C.; Granick, S. Anomalous yet Brownian. Proceedings of the National Academy of Sciences of the United States of America **2009**, 106, 15160–15164.

(59) Wierenga, A.; Philipse, A. P.; Lekkerkerker, H. N. W.; Boge, D. V. Aqueous Dispersions of Colloidal Boehmite: Structure, Dynamics, and Yield Stress of Rod Gels. Langmuir **1998**, 14, 55–65.

(60) Szamel, G. Reptation as a Dynamic Mean-Field Theory - Study of a Simple-Model of Rodlike Polymers. Physical Review Letters **1993**, 70, 3744–3747.